Additional file 1 for:

Estimating errors in autocorrelation functions for reliable investigations of reflection profiles

Yuta Maeda, Toshiki Watanabe

Text S1. Waveforms of shallow- and deep-focus earthquakes

Selecting earthquakes $\geq$ 80 km resulted in the clearest image at E.STHM (``Results'' section; Fig. 3d). Using earthquakes $\geq$ 60 km resulted in a less clear image than the results from $\geq$ 80 km, despite the increasing number of stacks, indicating that the number of stacks is not the only factor that affects the results; other factors consist of the length of the time window and simplicity of the waveforms. Fig. S1 shows the waveforms of earthquakes of similar magnitudes (2.7–2.9) sorted in depth order; Fig. S1a and b show the waveforms from Station E.STHM and N.SHMH, respectively. N.SHMH is located at a depth of 2.3 km; a downgoing wave reflected from the ground surface arrives at this station 1.8 s after the first arrival of the upgoing incident wave according to the P-wave velocity profile measured in this borehole (Ohta et al. 1978; Suzuki et al. 1983; Fig. 3a). The incident (upgoing) and reflected (downgoing) waves were dominant in the waveforms of $\geq$ 80 km earthquakes at N.SHMH, whereas long-lasting coda of relatively large amplitudes contaminated the waveforms of shallow-focus (60–80 km) earthquakes (Fig. S1b). Daylight imaging assumes an impulsive incident wave. Fig. S1b indicates that the incident wave was impulsive for deep ($\geq$ 80 km) earthquakes and was not impulsive for shallow (60–80 km) earthquakes. This difference seems to be attributed to near-source regions of earthquakes because the ray paths near the ground surface are almost identical. The foci of the shallow (60–80 km) earthquakes immediately below N.SHMH were clustered in a narrow region (Fig. 1), suggesting that the effect of the non-impulsive incident wave was not canceled by stacking.

Text S2. Tests using synthetic waveforms

Although the main text focused on real data, tests using synthetic waveforms are another approach to evaluate the method. We performed synthetic tests using a two-layer model composed of a sedimentary layer (P-wave velocity: V_1) underlain by the basement (P-wave velocity: V_2). We used $V_2 = 5$ km/s and an interface depth of 1.5 km and varied V_1. We used a Ricker wavelet with a time constant of 0.2 s for an incident wave that propagates upward from the lower side of the interface. Fig. S2aA shows the synthetic waveform on the ground surface calculated using $V_1 = 2$ km/s (Fig. S2aF); this structure is almost the same as that below N.SHMH (Fig. 3a). The signals labeled D_0 and R_1 are direct and single reflected waves, respectively. The wave repeats reflections at the ground surface and the sedimentary-basement interface, causing multiple reflected waves (R_2–R_5).

We added Gaussian noise to the simulated waveform; the noise level was controlled using the signal-to-noise (S/N) ratio, which varied from 3.0 (Fig. S2aB) to 1.5 (Fig. S2aC). This range of the S/N ratio was close to that of the observed waveforms; the S/N ratio was 2.87 for the largest (M4.5) earthquake and 1.75 for the deepest earthquake of the smallest magnitude (M2.0) at Station E.STHM. From these waveforms, we investigated the ACFs and errors using the proposed method (Fig. S2aD and aE). The single reflected wave was imaged at 1.5 s, and multiple reflected waves were imaged after 3.0 s. We converted the ACFs to reflection responses, divided the responses by standard deviations, and plotted the results on a depth section (Fig. S2aG). The green line in Fig. S2aF shows the relation between the lag time and depth, indicating that the multiple reflected waves after 3.0 s were out of the plotted depth range. Fig. S2aG shows a prominent reflector at a depth of 1.5 km with an amplitude substantially greater than three. In addition, minor peaks with amplitudes less than three were present at 0.8 km and 3.2 km; these peaks were caused by random noise and could be misinterpreted as reflectors if errors were not estimated. Our criterion of three successfully rejected these false reflectors (Fig. S2aG). The negative peaks at 1.4 km and 1.6 km and positive peaks at 1.3 km and 1.7 km in Fig. S2aG are side lobes of the main peak at 1.5 km caused by the bandpass filter. These side lobes are inevitable and need attention in the interpretation. Except for the side lobes, the detection threshold of three times the standard deviation worked to distinguish true and false reflectors in the case of $V_1 = 2$ km/s.

Fig. S2b shows the results from $V_1 = 4$ km/s. Although the reflector at a depth of 1.5 km was less prominent than in Fig. S2a, the amplitude of this reflector was still greater than the detection threshold (three). However, the amplitude was only slightly greater than three when 1.5 was used for the S/N ratio of the waveform (i.e., relatively noisy waveform; red). These results indicated that a discontinuity between 4 and 5 km/s can be detected with high confidence if the waveform has a high S/N ratio.

Fig. S2c shows the results from the structure at Station N.FCHH of Hi-net, where a borehole down to 2.75 km has been drilled (Yamamizu et al. 1981). The velocity discontinuities at 1.3 km and 2.0 km were imaged as reflectors with amplitudes significantly greater than three, although the spatial separation of these reflectors was not good due to the wavelength that was used (Fig. S2cG). The reflector that corresponds to the velocity discontinuity at a depth of 0.3 km was also prominent when the waveform has a high S/N ratio (Fig. S2cG, blue).

We systematically varied V_1 and the S/N ratio in the two-layer model. Fig. S3 shows the maximum value of the ratio of the reflection response to the standard deviation around a depth of 1.5 km by color; large circles represent ratios greater than three, meaning that the reflector at 1.5 km is detectable. Fig. S3 indicates that the velocity discontinuities with reflection coefficients greater than 0.03 and 0.1 were identified as true when waveforms with high and low S/N ratios were used, respectively.

Text S3. Covariance of the noise waveform

We generated $u_{i,j}^{noise}(t)$ (Eq. 2) by random values that independently obeyed a normal distribution; the correlation of $u_{i,j}^{noise}(t)$ for different t values were not considered. To minimize the correlation, we used a narrow bandwidth (0.0305 Hz) for the whitening (``Method for estimating the ACFs and errors" section). In this section, we evaluate how this approach works.

Fig. S4a shows the distribution of $u(t)u(t+\tau)$, where $u(t)$ is the waveform of Fig. 2c in the noise window. At $\tau = 0.020$ s, the values of $u(t)u(t+\tau)$ systematically deviated to the positive side, indicating that $u(t)$ and $u(t+\tau)$ were positively correlated. At $\tau = 0.060$ s, $u(t)u(t+\tau)$

slightly deviated to the negative side, indicating a weak negative correlation. The distribution was almost symmetric after $\tau = 0.080$ s. We evaluated the symmetricity by the number ratio of positive samples in $u(t)u(t+\tau)$ (Fig. S4b). This ratio was between 0.4 and 0.6 for 0.075 s $\leq \tau \leq$ 5.070 s, indicating that the distribution was almost symmetric in this range of τ. Fig. S4c shows the covariance normalized by the variance, which was between -0.3 and 0.3 for $\tau \geq$ 0.075 s. These results indicated that $u(t)$ and $u(t+\tau)$ were correlated in $\tau \leq 0.075$ s. This correlation may be attributed to the bandpass filter of 1–10 Hz; because this filter drops signals beyond 10 Hz, $u(t)$ is expected to correlate with $u(t+\tau)$ for $\tau \leq 0.1$ s. Except for this filtering effect, the correlation between $u(t)$ and $u(t+\tau)$ was small (Fig. S4).

Text S4. Statistical tests for the normal distribution approximation

We evaluated the normal distribution approximation for noise waveforms from the χ^2 test. We used the largest (M4.5) earthquake (Fig. 5a) and the deepest earthquake of the smallest (M2.0) magnitude (Fig. 5b) for the test. We used bins that have a width of one-fifth to the standard deviation of the amplitudes of each waveform, and counted the number of samples in each bin. We calculated

$$\chi^2 = \sum_k \left(n_k^{obs} - n_k^{exp}\right)^2 / n_k^{exp}, \quad \text{(S1)}$$

where n_k^{obs} and n_k^{exp} are the number of samples in kth bin and the number expected from the normal distribution, respectively. We used only bins with $n_k^{obs} \geq 5$ for calculating χ^2. Results are compared with a threshold value (χ_0^2) at which the upper cumulative probability of χ^2 distribution with $\nu - 1$ degrees of freedom is 0.05, where ν is the number of bins used in the calculation of Eq. (S1); $\chi^2 < \chi_0^2$ means that the assumption of the normal distribution is not dismissed at 5% significance level. Results from raw (Fig. 2a), whitened (Fig. 2b), and bandpass-filtered (Fig. 2c) waveforms in the noise window of the two earthquakes in Fig. 5a and b are summarized in Table S1. In the whitened waveforms, χ^2 were smaller than χ_0^2 for both earthquakes, showing that the assumption of the normal distribution was not dismissed. Table S1 also indicated that the assumption of the normal distribution was dismissed for the raw waveforms of both earthquakes and the filtered waveform of the smaller earthquake. These results show that $u_{i,j}^{noise}(t)$ (Eq. 2) needs to be generated after the whitening and before the bandpass-filtering.

We also performed Kolmogorov-Smirnov (KS) test for the same data. This test uses the cumulative distributions (Fig. 5a and b) directly and does not require bins. Let N be the number of samples, and D be the absolute maximum value of the difference between the cumulative probability of data and that expected from the normal distribution. The assumption of the normal distribution is not dismissed at 5% significance level if $D\sqrt{N} < 1.36$. Table S1 showed that the assumption of the normal distribution was not dismissed for the whitened waveforms of both earthquakes.

We also performed χ^2 and KS tests for ACFs (Fig. 5c and d). The tests were performed for each lag time τ independently, using the 1000 ACF amplitudes at the same τ, and results are plotted as functions of τ (Fig. S5). The assumption of the normal distribution is dismissed at 5% significance level if red lines are above blue lines. Fig. S5 indicated that the assumption of the normal distribution was not dismissed for most τ.

Table S1. Results of χ^2 and KS tests for noise waveforms.

Waveform type	χ^2	ν	χ_0^2	$D\sqrt{N}$
Largest (M4.5) earthquake				
Raw	54.723	26	37.652	0.938
Whitened	29.326	26	37.652	0.579
Bandpass-filtered	36.788	26	37.652	1.909
Deepest earthquake of smallest (M2.0) magnitude				
Raw	55.633	26	37.652	1.997
Whitened	27.405	26	37.652	0.730
Bandpass-filtered	89.444	25	36.415	1.803

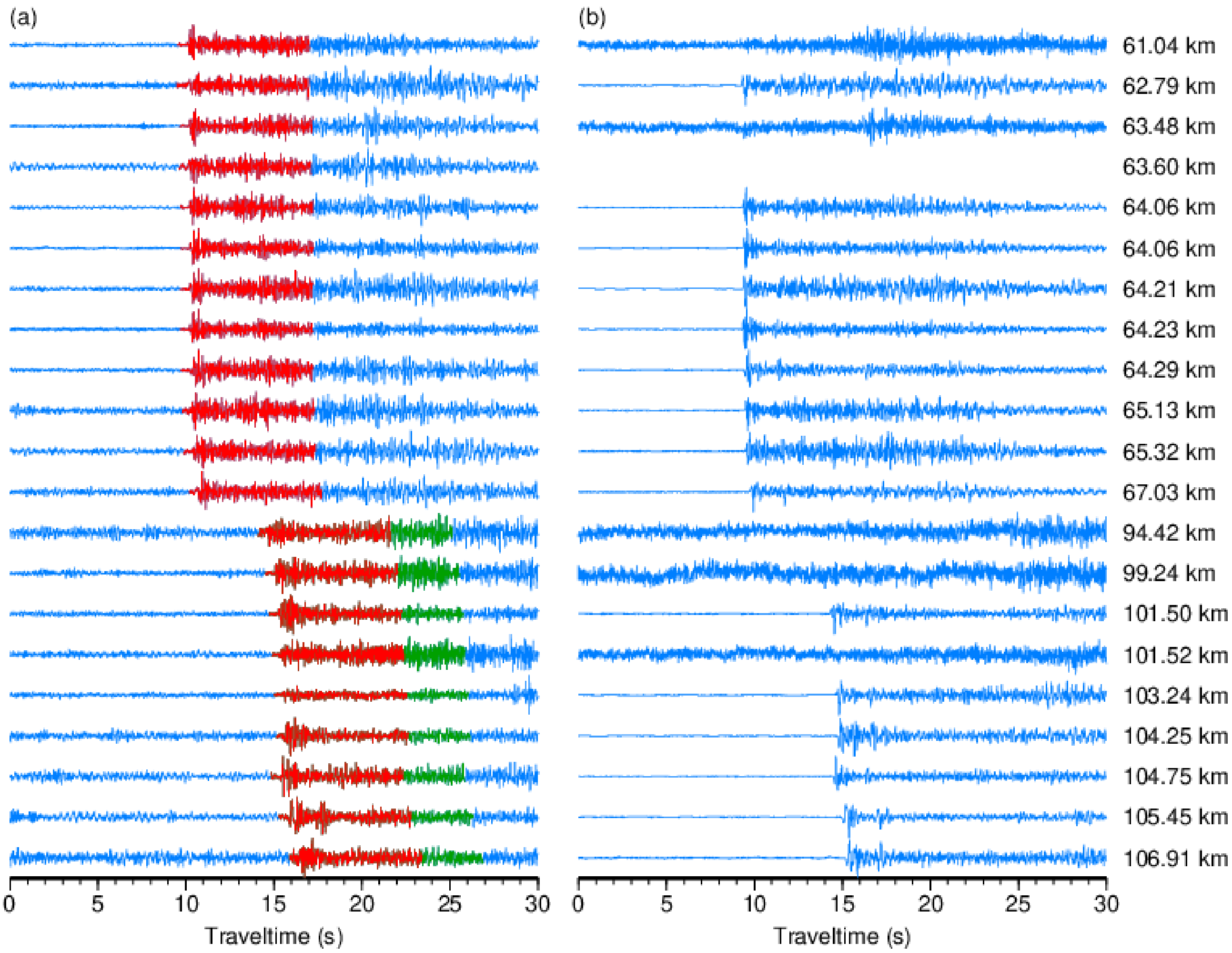

Fig. S1. Waveforms of M2.7–2.9 earthquakes used to compute the ACF at E.STHM. (a) Raw waveforms at E.STHM. Red and green represent time windows from 0.5 s before to 7.0 s and 9.5 s after T_p, respectively; these time windows were used for the P-wave windows in the analyses for $\geq$ 60 km and $\geq$80 km earthquakes. (b) Raw waveforms at N.SHMH. The focal depths of earthquakes are shown on the right.

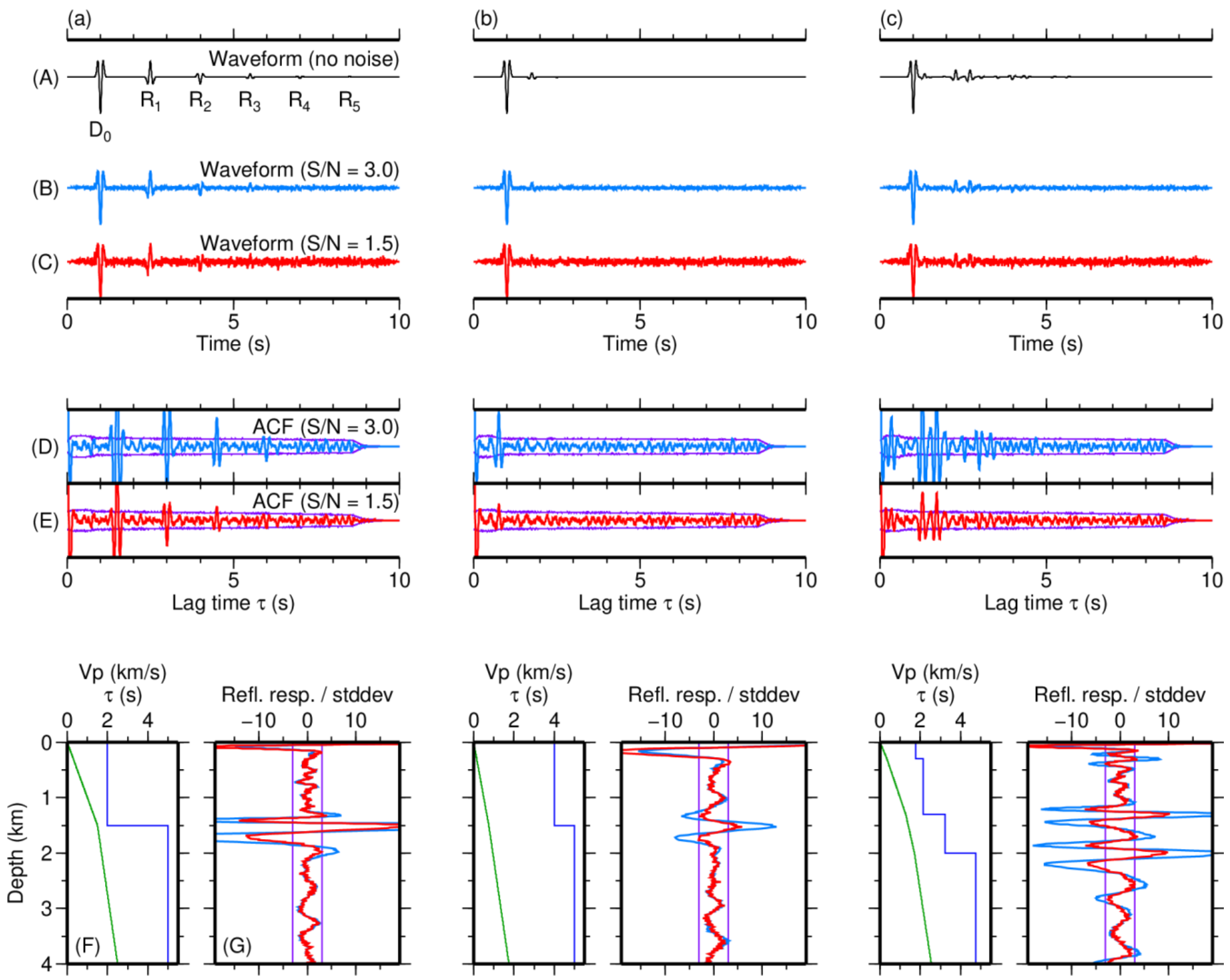

Fig. S2. Tests using synthetic waveforms. (a) Results from a two-layer model with $V_1 = 2$ km/s and $V_2 = 5$ km/s, (b) $V_1 = 4$ km/s and $V_2 = 5$ km/s, and (c) the velocity structure at Station N.FCHH of Hi-net (Yamamizu et al. 1981). (A) Synthetic waveform without noise, (B) with a small amount of noise (S/N ratio: 3.0), and (C) with a large amount of noise (S/N ratio: 1.5). D_0 represents the direct wave, and R_1–R_5 represents reflected waves; the subscript represents the number of reflections at the velocity discontinuity. (D)(E) ACFs calculated with the proposed method for the small and large noise scenarios. Purple lines represent three times the standard deviation. (F) Subsurface structure used to compute the synthetic waveform (blue) and the relationship between the lag time τ and depth (green). (G) Depth section of the reflection response from Fig. S2D and E plotted by blue and red, respectively; the ratios of the response to the standard deviation are plotted, and the values of ± 3 are shown by black lines.

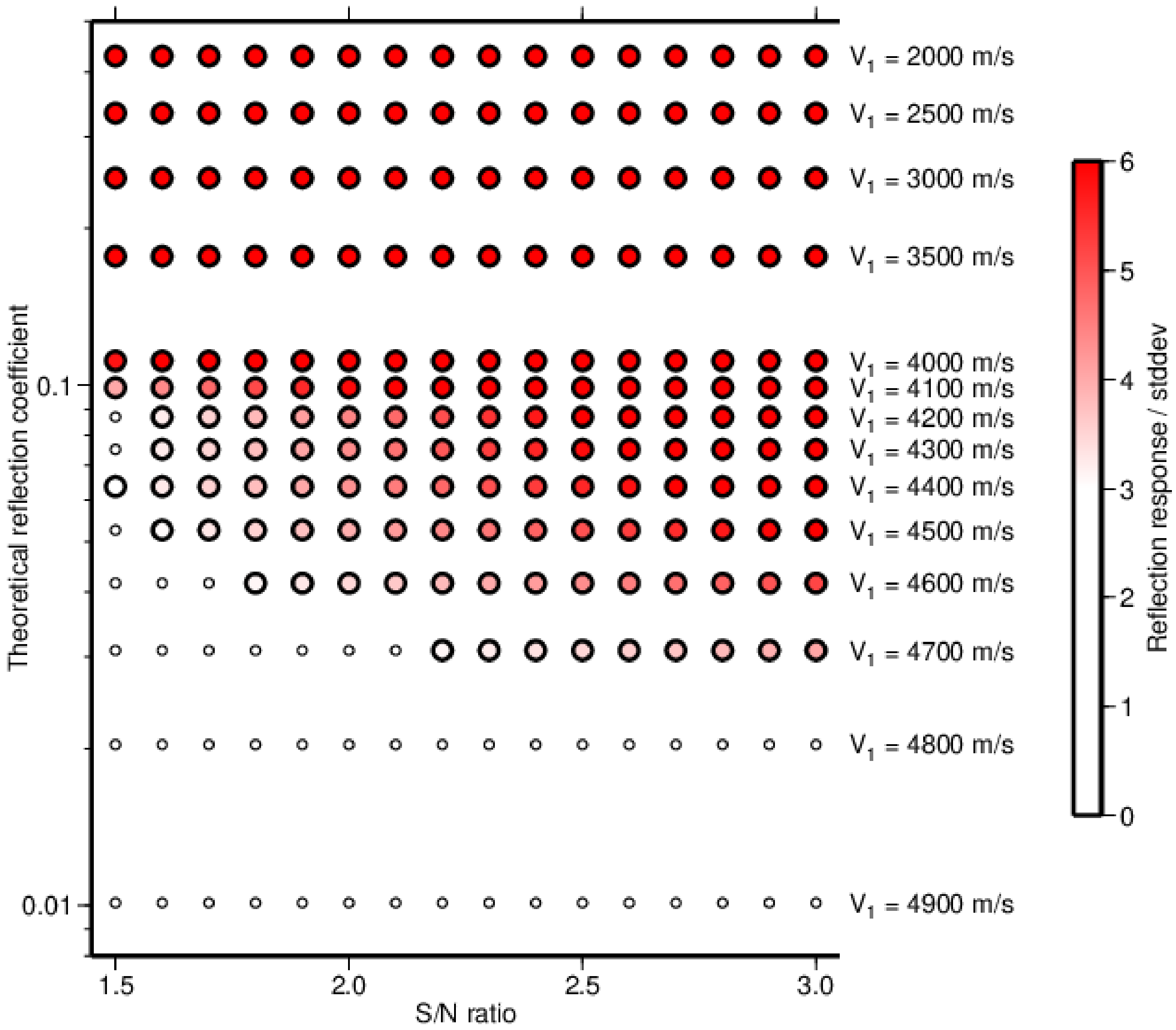

Fig. S3. Summary of the results of synthetic tests. A two-layer model with $V_2 = 5$ km/s and various V_1 was used. The color represents the maximum amplitude of the ratio of the reflection response to the standard deviation around a depth of 1.5 km; large circles show values greater than three.

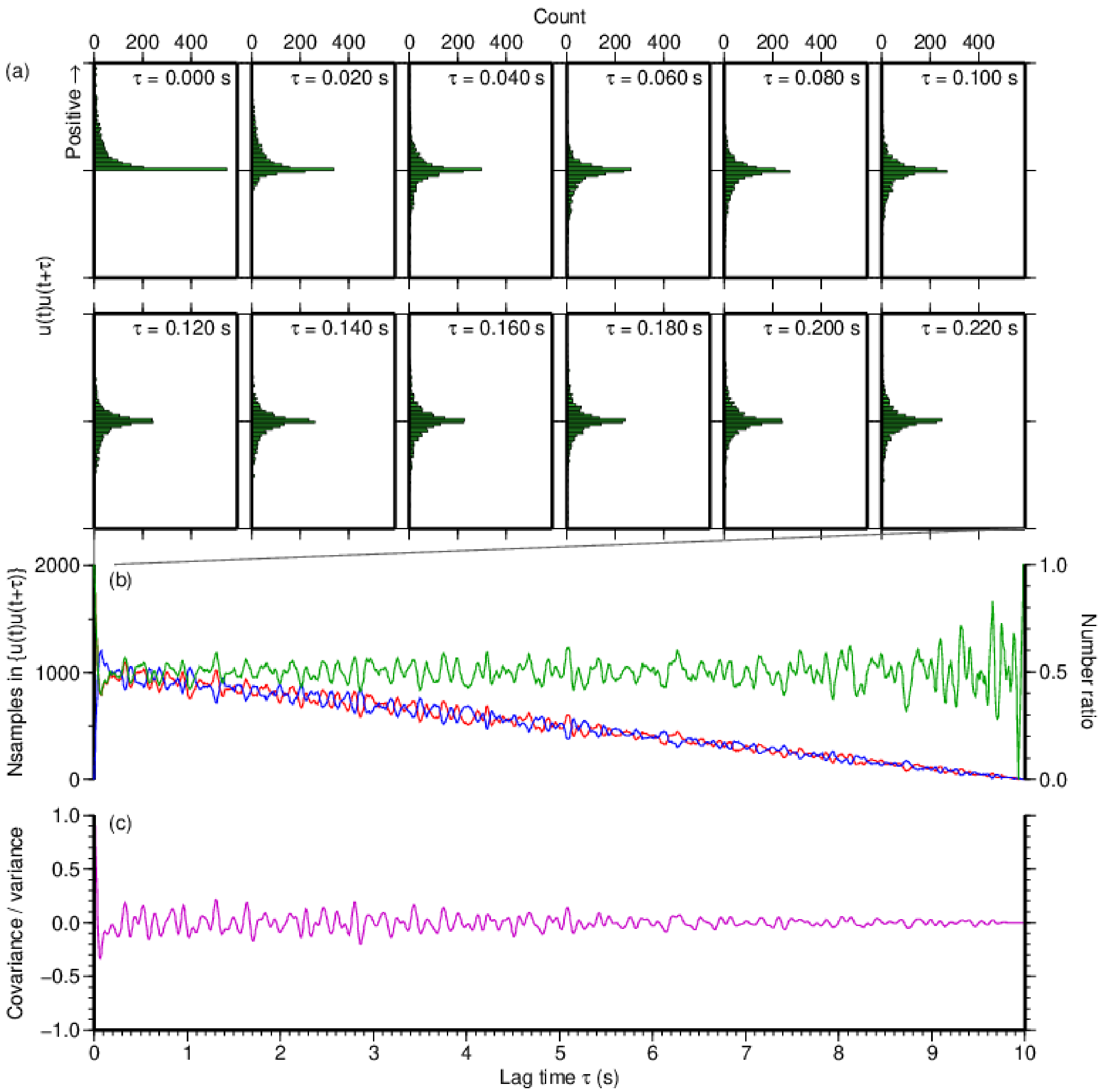

Fig. S4. Evaluation of the covariance of the waveform in the noise window from Fig. 2c. (a) Histograms of $u(t)u(t+\tau)$ for various τ values. (b) Numbers of positive (red) and negative (blue) samples in $u(t)u(t+\tau)$ and the number ratio of positive samples (green). (d) Covariance of $u(t)$ plotted versus τ.

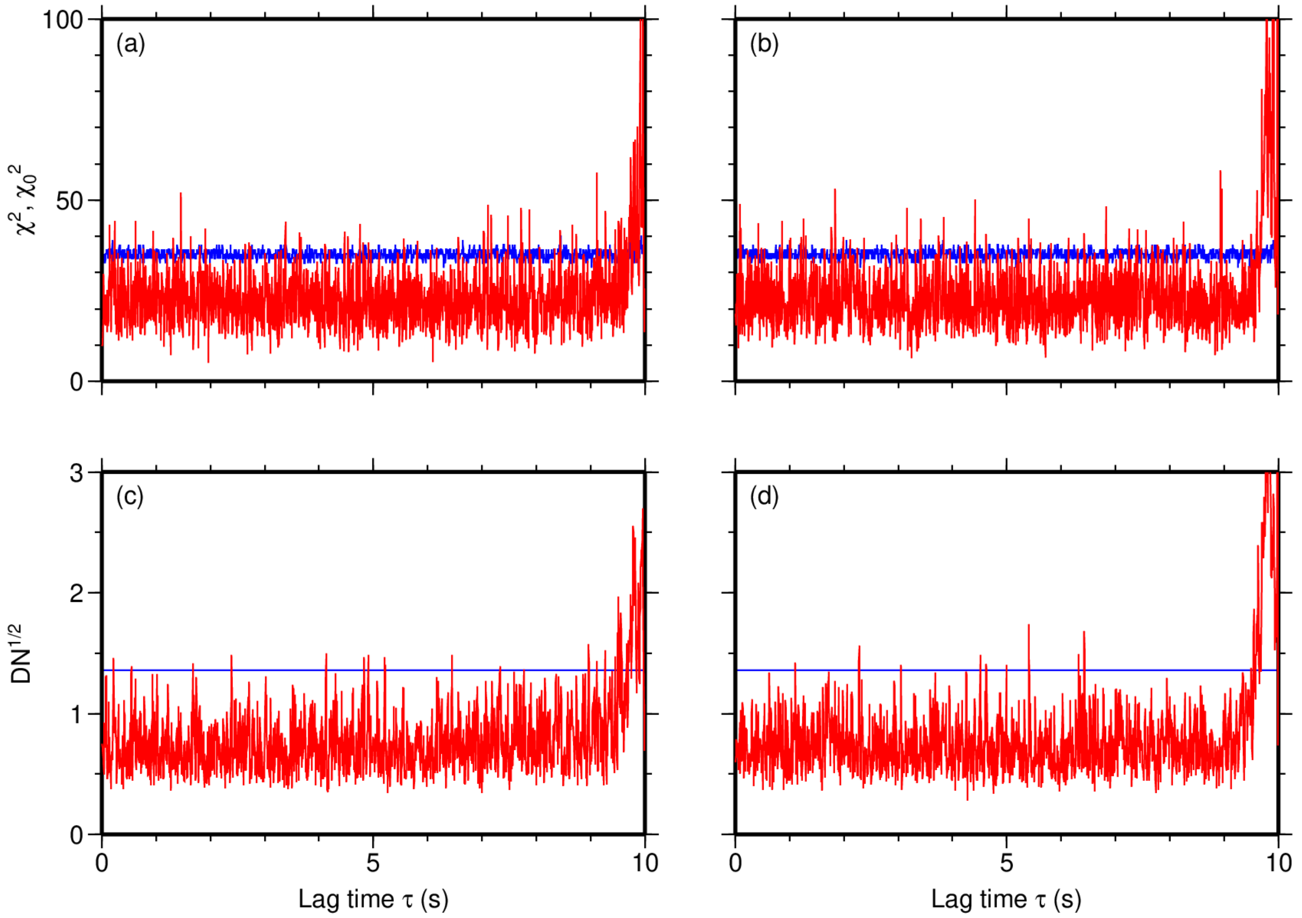

Fig. S5. Results of χ^2 and KS tests for ACFs. (a)(b) Results of χ^2 tests. Red and blue lines show χ^2 and χ_0^2 for 5% significance level, respectively. (c)(d) Results of KS tests. Red and blue lines show $D\sqrt{N}$ and 1.36 (a threshold for 5% significance level), respectively. The results for the largest (M4.5) earthquake are shown in Fig. S5a and c; those for the deepest earthquake of the smallest (M2.0) magnitude are shown in Fig. S5b and d.